





Control of second-harmonic generation in all-dielectric intersubband metasurfaces by controlling the polarity of $\chi^{(2)}$

RAKTIM SARMA,^{1,2,6,*} JIAMING XU,^{3,6} DOMENICO DE CEGLIA,⁴
LUCA CARLETTI,⁴  JOHN KLEM,¹ MIKHAIL A. BELKIN,^{3,5}  AND
IGAL BRENER^{1,2,7}

¹Sandia National Laboratories, Albuquerque, New Mexico 87123, USA

²Center for Integrated Nanotechnologies, Sandia National Laboratories, Albuquerque, New Mexico 87123, USA

³Department of Electrical and Computer Engineering, University of Texas at Austin, Austin, Texas 78712, USA

⁴Department of Information Engineering & INO-CNR, University of Brescia, Brescia 25121, Italy

⁵Walter Schottky Institute, Technical University of Munich, Garching 85748, Germany

⁶Equal contributions.

⁷ibrener@sandia.gov

*rsarma@sandia.gov

Abstract: All-dielectric metasurfaces have recently led to a paradigm shift in nonlinear optics as they allow for circumventing the phase matching constraints of bulk crystals and offer high nonlinear conversion efficiencies when normalized by the light-matter interaction volume. Unlike bulk crystals, in all-dielectric metasurfaces nonlinear conversion efficiencies primarily rely on the material nonlinearity, field enhancements, and the modal overlaps, therefore most efforts to date have only focused on utilizing these degrees of freedom. In this work, we demonstrate that for second-harmonic generation in all-dielectric metasurfaces, an additional degree of freedom is the control of the polarity of the nonlinear susceptibility. We demonstrate that semiconductor heterostructures that support resonant nonlinearities based on quantum-engineered intersubband transitions provide this new degree of freedom. We can flip and control the polarity of the nonlinear susceptibility of the dielectric medium along the growth direction and couple it to the Mie-type photonic modes. Here we demonstrate that engineering the $\chi^{(2)}$ polarity in the meta-atom enables the control of the second-harmonic radiation pattern and conversion efficiency. Our results therefore open a new direction for engineering and optimizing second-harmonic generation using all-dielectric intersubband nonlinear metasurfaces.

© 2022 Optica Publishing Group under the terms of the [Optica Open Access Publishing Agreement](#)

1. Introduction

Ever since the invention of the laser, one of the most prominent nonlinear optical processes that has been studied to date is second-harmonic generation (SHG) as it has a wide range of applications ranging from spectroscopy [1], imaging [2], sensing [3], to quantum optics [4,5]. Conventional approaches for SHG rely on using high power lasers and nonlinear bulk crystals with relatively large magnitude of second-order nonlinear susceptibility $\chi^{(2)}$. Since bulk crystals are subject to phase matching requirements, depending on the geometry, different techniques are utilized for efficient SHG. For example, in the case of optical waveguides, one way to achieve phase matching is using the birefringence of the nonlinear crystals combined with modal dispersion engineering [6]. Another technique, which gives very high SHG efficiency, is to modify the crystal to have regions of periodic domains with alternating $\chi^{(2)}$ polarity. While the latter approach does not allow a perfect phase matching between the fundamental and the second-harmonic signal, it

nevertheless can boost the interaction length by periodic compensation of the phase-mismatch between pump and second-harmonic fields, and it is referred to as quasi-phase matching [6–9].

Recently, all-dielectric metasurfaces have changed the way we think about SHG in photonic structures. These all-dielectric metasurfaces have thicknesses that are comparable or smaller than the incident pump wavelength and efficient SHG is achieved in subwavelength thicknesses by resonantly enhancing the interacting fields, without the requirement of phase matching [10–18]. The absence of phase matching constraints allows metasurfaces to operate without any stringent angular alignment requirements with respect to the incident beam. So far, the SHG efficiencies from all-dielectric metasurfaces have primarily relied on the material nonlinearity [12,14], field enhancements [12–14,16–19], and modal overlap optimization [20]. Quasi-phase matching techniques based on periodic modulation of the $\chi^{(2)}$ polarity have not been yet investigated in all-dielectric metasurfaces. On one hand, poling techniques are conventionally used in bulk configurations, on the other hand, it is not straightforward to control at the subwavelength scale the polarity of the second order nonlinear susceptibility $\chi^{(2)}$ in conventional materials, such as GaAs [12,13,16,21–23], AlGaAs [14,15,18,24,25], Silicon [17], GaP [19] or LiNbO₃ [4], used for fabricating nonlinear all-dielectric metasurfaces. One aspect of all-dielectric metasurfaces that so far has been ignored is that the polarity of $\chi^{(2)}$ along the growth direction (z axis) determines the polarity of the z -component of the second-harmonic nonlinear polarization which in turn determines the spatial profile of the photonic mode being excited at the second-harmonic wavelength. Since the spatial profile of the photonic mode at the second-harmonic wavelength determines the radiation pattern and the efficiency of SH emission [25], the spatial variation of the polarity of $\chi^{(2)}$ along z can modify the overall SHG efficiency of a nonlinear metasurface. This is especially relevant for all-dielectric metasurfaces that support Mie-type modes, which are volume modes with a wide range of spatial field profiles and polarization depending on the shape, size, and symmetry of the meta-atoms [16–19,26–28].

In this paper, we explore the role of the sign or polarity of the nonlinear susceptibility of the dielectric medium constituting the meta-atoms for controlling SHG using all-dielectric metasurfaces that support Mie-type photonic modes. We demonstrate that by controlling the polarity of $\chi^{(2)}$ along the growth direction (z axis), we can control the overall SHG radiation pattern of the meta-atoms and the conversion efficiency of the nonlinear metasurface. To modulate the polarity of the $\chi^{(2)}$ along the growth direction, we design a semiconductor heterostructure that supports doubly resonant nonlinearities using quantum engineered intersubband transitions (ISTs). While the giant magnitudes of such nonlinearities have been utilized before to achieve record high SHG efficiency using plasmonic metasurfaces and all-dielectric metasurfaces [29–34], in this work, we vary the polarity of $\chi^{(2)}$ along the growth direction to control the SHG efficiency. We use the technique of spatial inversion in the growth sequence of two coupled asymmetric quantum-wells (QWs) to flip the signs of the transition dipole moments of the ISTs. This technique leads to flipping of the polarities of the real and imaginary parts of $\chi^{(2)}$ of the nonlinear medium. As proof-of-concept, using this technique, we demonstrate experimentally that we can increase or decrease the second-harmonic generation efficiency of the metasurface by 5 times. Besides being fundamentally new, our results open a new direction of utilizing the polarity of $\chi^{(2)}$ as an additional degree of freedom to control the SHG efficiency of all-dielectric metasurfaces. Our results can be of significance especially for multimodal high aspect ratio Mie type structures [24,35] where the structures support several modes along the vertical direction. Our presented method can also open new directions for controlling the SHG efficiency to develop new classical or quantum light sources based on efficient nonlinear optical processes such as SHG or spontaneous parametric down conversion [4,5] as well as for developing compact and efficient light sources at mid- to long-infrared region of the electromagnetic spectrum for numerous applications including sensing [3], spectroscopy [1], and hyperspectral infrared imaging [2].

2. Working principle of the all-dielectric nonlinear intersubband metasurface

A schematic of the nonlinear all-dielectric metasurfaces used in this study is shown in Fig. 1(a). The metasurfaces consist of periodically spaced cylindrical dielectric resonators fabricated from III-V semiconductor heterostructures with *n*-doped In_{0.53}Ga_{0.47}As/Al_{0.52}In_{0.48}As multi-QWs. The resonators are placed on top of a Sapphire substrate with a lower refractive index SiO₂ cap on top. The multi-QW heterostructure is optimized to support three equally spaced energy levels with energy separation of approximately 156 meV (7.8 μm). In our asymmetric coupled QW structure, we chose the length of the Al_{0.52}In_{0.48}As barriers such that the coupling between adjacent QW structures is minimal. A three-level electronic system in an asymmetric coupled-QW design is used as it enables optical transitions at both the fundamental pump wavelength (7.8 μm) and second harmonic (SH) wavelength (3.9 μm) and thereby create a quantum system with a doubly-resonant $\chi^{(2)}$ for SHG which is known to have a larger magnitude compared to a singly-resonant $\chi^{(2)}$ [36]. Figure 1(b) shows an example of an 8-band k.p band structure calculation of the conduction band of a single period of one of multi-QW systems used in this study. In such a QW system and because of the selection rules, only out-of-plane polarized electric fields can couple to the ISTs and therefore the only non-zero element of the $\chi^{(2)}$ -tensor in such a system is $\chi_{zzz}^{(2)}$ which can be approximated at low pumping intensities as [33,37] :

$$\chi^{(2)} = \frac{e^3}{\epsilon_0 \hbar^2} \frac{N_d z_{12} z_{23} z_{31}}{(\omega - \omega_{12} - i\gamma_{12})(2\omega - \omega_{13} - i\gamma_{13})}, \quad (1)$$

where e is the elementary charge, ϵ_0 is the vacuum permittivity, \hbar is the reduced Plank constant, N_d is the average bulk doping density, and γ_{ij} represent the IST damping rate; $e z_{ij}$ are the transition dipole moments between levels i and j and their magnitudes for the optimized QW structure used in this study are found to be $|z_{12}| = 1.6$ nm, $|z_{23}| = 1.99$ nm and $|z_{31}| = 0.92$ nm using band structure calculations.

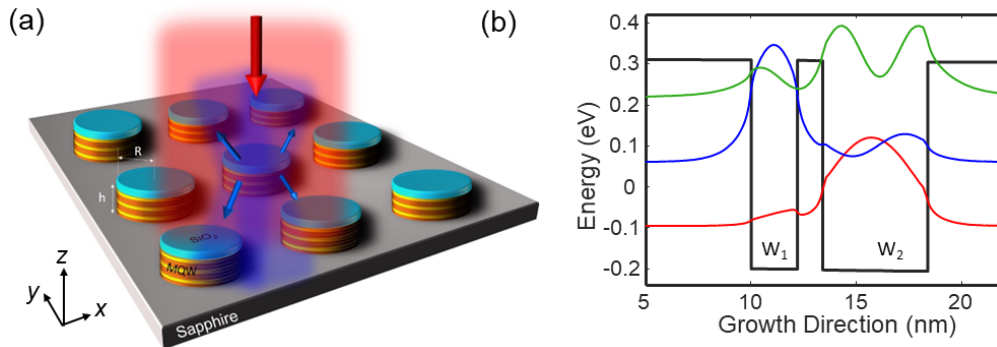


Fig. 1. Schematic and working principle of the all-dielectric intersubband metasurfaces with different polarities of $\chi^{(2)}$. (a) Schematic of the nonlinear metasurface. The height (h) of all the fabricated cylindrical Mie resonators is 1.5 μm. The radii (R) of the cylinders are varied to modify the spectral position of the Mie resonances. (b) 8 band k.p calculation of the conduction band of a single period of one of the asymmetric coupled QW structure used in this study. The thicknesses of the two asymmetric coupled QWs are optimized to support three equally spaced energy levels separated by 156 meV (7.8 μm) so that the heterostructure can generate second harmonic (SH) signal at 312 meV (3.9 μm). The layer structure of a single period of the heterostructure is given as **10 nm/5 nm/1.2 nm/2.2 nm/10 nm**, where Al_{0.52}In_{0.48}As barriers are shown in bold and the two In_{0.53}Ga_{0.47}As wells (W_1 and W_2) are shown in a regular font. All In_{0.53}Ga_{0.47}As layers are *n*-doped with doping density of $2 \times 10^{18} \text{ cm}^{-3}$.

As shown in Eq. (1), an interesting property of such a system is that $\chi_{zzz}^{(2)}$ is proportional to the product of three dipole moments (ez_{ij}). This implies that the polarity of $\chi_{zzz}^{(2)}$ can be reversed by spatially inverting the multi-QW structure along the growth direction z as that will flip the polarity of the transition dipole moments z_{ij} . Figure 2(a) shows the growth scheme we implemented to generate multi-quantum well heterostructures with opposite polarities of $\chi^{(2)}$; the calculated real and imaginary components of $\chi_{zzz}^{(2)}$ for the QW structures are shown in Fig. 2(b, c). We can clearly see that both structures have equal magnitude of $\chi_{zzz}^{(2)}$ but with opposite polarities.

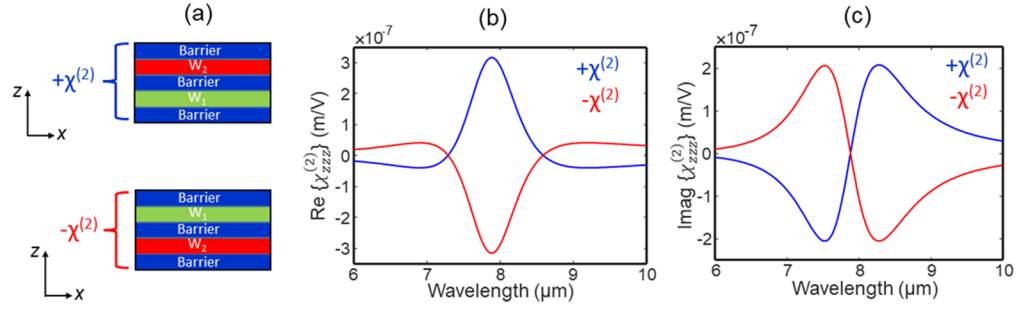


Fig. 2. Scheme to generate multi-QW heterostructures with opposite polarities of $\chi^{(2)}$. (a) Schematic showing cross section along the x - z plane of two heterostructures which are inverted with respect to one another along the growth direction z . W_1 and W_2 correspond to the two $\text{In}_{0.53}\text{Ga}_{0.47}\text{As}$ quantum wells shown in Fig. 1(b). Since $\chi_{zzz}^{(2)}$ is proportional to the product of the three transition dipoles corresponding to three ISTs, to flip the sign of real and imaginary part of $\chi_{zzz}^{(2)}$, we spatially invert the structure by flipping the growth sequence along z which leads to flipping of the signs of the transition dipole moments of the ISTs. (b, c) Calculated value of the real (b) and imaginary (c) part of intersubband nonlinear susceptibility of the multi-QW structure shown in Fig. 1(b) and the flipped/inverted structure as a function of the pump wavelength. As shown, the polarities are flipped with respect to one another for both cases.

While flipping the growth sequence alters the polarity of $\chi_{zzz}^{(2)}$, it does not affect the linear dielectric permittivity of the medium. This is because, the multi-QW heterostructure embedded in the nanoresonators can be approximated as a homogeneous, anisotropic layer with dielectric-constant tensor $\epsilon_{\text{QW}} = \epsilon_t(\hat{x}\hat{x} + \hat{y}\hat{y}) + \epsilon_l\hat{z}\hat{z}$, where the transverse dielectric constant is $\epsilon_t = 11.08$ and the longitudinal dielectric constant can be approximated as [33]:

$$\epsilon_l = 11.08 + \frac{f_{12}\omega_{12}^2}{\omega_{12}^2 - \omega^2 - 2i\omega\gamma_{12}} + \frac{f_{13}\omega_{13}^2}{\omega_{13}^2 - \omega^2 - 2i\omega\gamma_{13}}, \quad (2)$$

where the first Lorentzian term in Eq. (2) models the first IST at $7.8 \mu\text{m}$ ($\omega_{12} = 2\pi \times 38.4 \times 10^{12}$ rad/s) and the second term models the second IST at the SH wavelength of $3.9 \mu\text{m}$ ($\omega_{13} = 2\pi \times 76.8 \times 10^{12}$ rad/s). The terms γ_{12} and γ_{13} represent the IST damping rate and the terms f_{12} and f_{13} are the oscillator strengths. While f_{12} and f_{13} do depend on the transition dipole moments, they do not change signs when the structure is reversed because these terms are proportional to square of the transition dipole moment. This unique property is important as it allows us to design and optimize the photonic structures to maximize coupling of the pump light to the ISTs regardless of the growth sequence.

As we recently demonstrated in [33], to achieve high SHG conversion efficiency, we optimized the dimensions of the cylinders such that they support a magnetic dipole (MD) mode at a wavelength that is slightly detuned from the fundamental IST wavelength ($7.8 \mu\text{m}$) but still within the linewidth of the IST resonance (Fig. 3(a)). The metasurface periodicity (p) was fixed at $3R$

to limit near-field coupling effects between neighboring meta-atoms. Under these conditions, the resonant wavelengths of the Mie modes depend on the geometric parameters of the single cylinders. We thus optimized the structure to support the MD mode at the desired wavelength by tuning the aspect ratio of the cylinders which is given by the ratio of radius (R) to height (h). In our study we kept the height constant at a value of $1.5\ \mu\text{m}$. Figure 3(a) shows the numerically calculated multipolar decomposition of the optimized metasurface. The metasurface with $R/h = 0.93$ supports a MD mode slightly detuned from the IST at $7.8\ \mu\text{m}$. The MD mode was chosen as it supports strong z -directed electric field components which are required by the selection rules of ISTs for efficiently coupling normally incident pump light to the ISTs (Fig. 3(b)) [33,38].

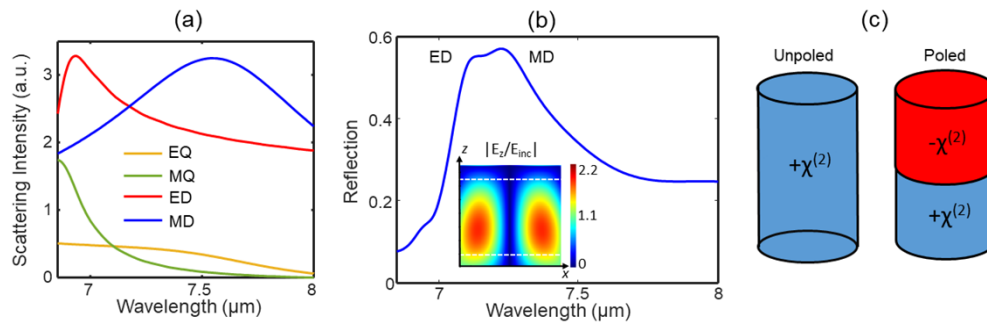


Fig. 3. Finite-difference time domain linear numerical simulation of the all-dielectric nonlinear metasurface. (a) Numerically calculated multipolar decomposition of a metasurface with cylindrical meta-atoms with $R/h = 0.93$ and $h = 1.5\ \mu\text{m}$. The resonators are optimized to support a magnetic dipole (MD) mode slightly spectrally detuned from the IST at $7.8\ \mu\text{m}$. MD, ED, MQ, and EQ correspond to magnetic dipole, electric dipole, magnetic quadrupole, and electric quadrupole modes, respectively. (b) Finite-difference-time domain simulation results of reflectance from a metasurface with cylinders of $R/h = 0.93$ and $h = 1.5\ \mu\text{m}$. The simulation includes the effect of ISTs on the real and imaginary parts of the dielectric constant of the multi-QW layer. The inset shows the magnitude of the field enhancement of the z component of the electric field $|E_z/E_{inc}|$ at the IST wavelength of $7.8\ \mu\text{m}$. The out-of-plane (E_z) field components allow for efficient coupling of the normally incident pump light to the ISTs. The two dashed white lines indicate the regions where the multi-QWs are present within the meta-atoms. (c) Schematic of the unpoled (blue) and poled (blue and red) cylindrical meta-atoms studied in this work. The unpoled meta-atoms consists of nonlinear medium with only one polarity whereas the poled structure consists of nonlinear media with both polarities each filling half of the meta-atoms.

To demonstrate the effect of polarity switching of $\chi^{(2)}$ on SHG, as proof-of-concept, we studied two types of metasurfaces. The first one was comprised of *unpoled* meta-atoms which consisted of multi-QWs with the same polarity of $\chi^{(2)}$ (Fig. 3(c)). The second metasurface comprised of *poled* meta-atoms which consisted of two stacks of multi-QWs with opposite polarities of $\chi^{(2)}$ with both polarities filling up half the volume of the meta-atoms (Fig. 3(c)). The minimum poling period in these intersubband metasurfaces is determined by the period of the asymmetric coupled QW structure. In our case, the period of the asymmetric coupled QW structure used in this study is only $\sim 28.4\ \text{nm}$ which is much smaller compared to the second-harmonic wavelength. For a given pump and second-harmonic wavelength, we therefore can easily design our heterostructures such that there can be multiple periods of the asymmetric coupled QW structure to achieve poling. For both metasurfaces, the height h and the aspect ratio of the meta-atoms (R/h) are the same. As described above, since the linear dielectric permittivity for both cases is expected to be the same, in both cases, the spatial profile and resonant wavelength of the MD photonic mode supported by

the meta-atoms will be similar. However, since the nonlinear SH source or nonlinear polarization $J_z^{SH} = i2\omega\epsilon_0\chi^{(2)}E_z^2$ is proportional to $\chi^{(2)}$, the spatial distribution of J_z^{SH} within the meta-atoms for both cases will be different. In fact, compared to the *unpoled* meta-atoms, which will have J_z^{SH} with even symmetry along with the z -axis, the *poled* meta-atoms will have J_z^{SH} with odd symmetry along the z -axis. Since for both the metasurfaces, the meta-atoms support multiple modes at the SH wavelength (the SH wavelength is smaller compared to pump wavelength), the SH mode or superposition of modes that are being excited at the SH wavelength will be different in the unpoled and poled metasurfaces as it will be determined by the spatial distribution of J_z^{SH} within the meta-atoms. This will lead to overall different SHG efficiencies.

3. Numerical simulations and experimental results

To observe the effect of polarity switching of $\chi^{(2)}$ on SHG efficiency, we first performed nonlinear numerical simulations using the frequency domain implemented with the finite-element method in COMSOL. The resonant nonlinear susceptibilities of the multi-QW, $\chi_{\text{QW}}^{(2)} = \chi^{(2)}\hat{z}\hat{z}\hat{z}$, were modeled based on Eq. (1) and the linear permittivity of the multi-QW heterostructure was modeled based on Eq. (2). For the sapphire substrate and SiO₂ cap, we used experimentally measured quantities by ellipsometry. The nonlinear simulations were done in the undepleted pump approximation and neglecting saturation effects of the ISTs. The metasurface was assumed to be an infinite periodic array. Further details on the nonlinear simulation technique can be found in Ref. [34].

We analyzed second-harmonic light emission from both isolated meta-atoms and from metasurfaces. Figure 4(a) shows a comparison of the calculated spatial distribution of J_z^{SH} within *poled* and *unpoled* meta-atoms. As shown in Fig. 4(a), while the magnitude of J_z^{SH} within the meta-atoms for both cases are the same, the sign of J_z^{SH} in the *poled* meta-atom switches at the center, thus following the polarity of the $\chi^{(2)}$. Interestingly, because of the different spatial distributions of J_z^{SH} , the far-field SH emission patterns (shown in Fig. 4(b)) from the poled and unpoled isolated meta-atoms are very different. The *unpoled* meta-atom, because of dipole-like distribution of J_z^{SH} with even symmetry, emits the SH signal much more efficiently in the upward or reflection direction (emission into a semi-hemisphere centered around + z direction) compared to the *poled* meta-atom which has a quadrupole-like distribution of J_z^{SH} with odd-symmetry (see Fig. 4(a)).

To quantify the difference in SHG efficiencies for both cases, we also calculated the normalized SHG conversion efficiencies as a function of pump wavelength for metasurfaces made of arrays of poled and unpoled meta-atoms. The SHG conversion efficiency was calculated by collecting the SH light emitted in all the diffraction orders in reflection (air side). Figure 4(c) compares the calculated reflected SH efficiencies for *poled* and *unpoled* metasurfaces with $R/h = 0.93$ and 0.87 and with periodicities equal to three times the size of the meta-atom radius. As expected, we can clearly see that *poled* metasurfaces, for a wide range of pump wavelengths across the IST resonance, have lower SH efficiencies compared to *unpoled* metasurfaces. The exact magnitude of difference in SHG efficiencies between *poled* and *unpoled* metasurfaces depends on the aspect ratio of the cylindrical meta-atoms.

To confirm our predictions, we fabricated the designed metasurfaces and performed the linear and nonlinear experiments. We grew the designed and optimized heterostructures on a semi-insulating InP substrate using molecular beam epitaxy. The heterostructure comprised of multiple repetitions of the asymmetric coupled In_{0.53}Ga_{0.47}As QWs sandwiched between Al_{0.52}In_{0.48}As barrier layers as shown in Fig. 1(b). To flip the polarity of $\chi^{(2)}$ along the growth direction, we flipped the sequence of growth of the multi-QW structure after growing half the thickness (this corresponds to inverting the structure along z as shown in Fig. 2(a)) and the total thickness of the multi-QW stack that was grown was 852 nm. Since the MD mode is supported by cylindrical resonators of $R/h = 0.93$, we added additional Al_{0.52}In_{0.48}As layers symmetrically on

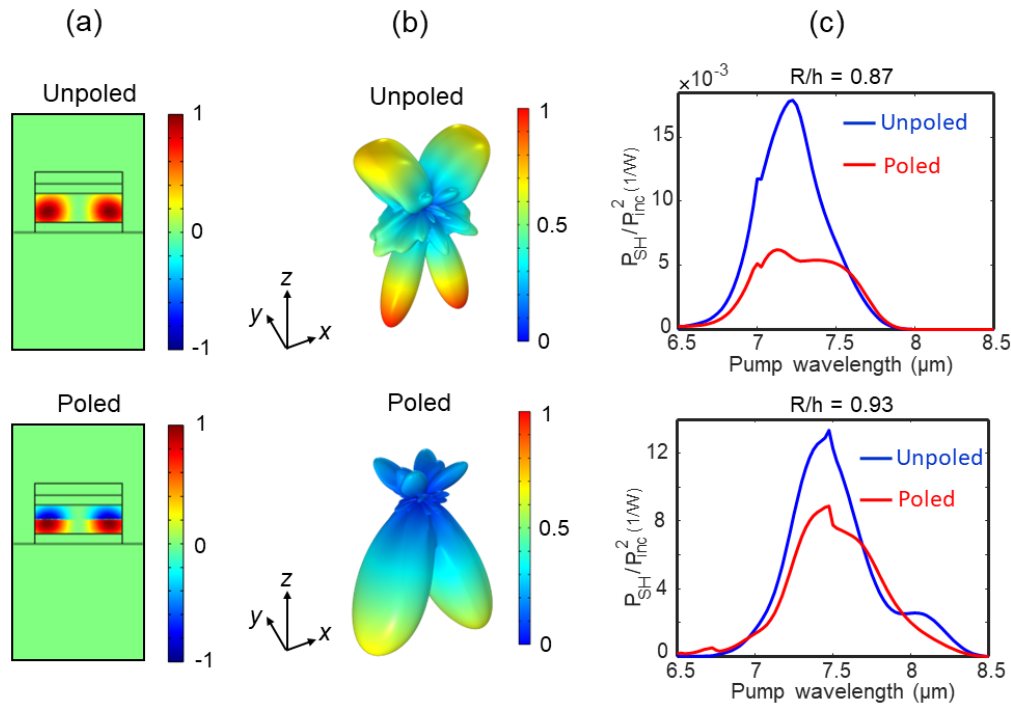


Fig. 4. Nonlinear numerical simulations of the metasurfaces comprised of the poled and unpoled meta-atoms (a) Numerically calculated spatial distribution of the nonlinear polarization J_z^{SH} in the x - z plane of the poled and unpoled meta-atoms with $R/h = 0.93$ and $h = 1.5 \mu m$. The unpoled meta-atom has nonlinear polarization of only one sign/polarity whereas in the poled structure the sign of the nonlinear polarization flips at the center of the meta-atom following the sign of the nonlinear susceptibility. (b) Three-dimensional far-field SH emission pattern of isolated poled and unpoled meta-atom structures with $R/h = 0.93$ (Radius (R) = $1.4 \mu m$). Because of the different distributions of the nonlinear polarization, as shown, the poled structure emits SH much less efficiently in reflection compared to the unpoled structure. (c) Comparison of numerically calculated reflected normalized SH power conversion efficiency from metasurfaces with poled and unpoled meta-atoms with $R/h = 0.93$ and 0.87 and periodicity equal to three times the radius of the meta-atom. Metasurfaces with poled meta-atoms in general have lower SHG efficiency compared to unpoled meta-atoms. The absolute magnitude of difference in SHG efficiency between the poled and unpoled metasurfaces depend on the exact aspect ratio of cylindrical meta-atoms.

top and bottom of the multi-QW stack to make the total epilayer thickness equal to $1.5 \mu m$. The epilayer thickness determined the height (h) of the resonators used in this study. After growth, the wafer was flipped and adhesively bonded to a Sapphire substrate using Benzocyclobutene. Following bonding, we removed the InP substrate by selective wet etching to leave the epilayer on top of the sapphire substrate. We chose Sapphire because of its optical properties (low absorption at the pump and second-harmonic wavelengths) and lower refractive index compared to the QW heterostructure which is needed for the metasurface to support Mie modes. Furthermore, the thermal expansion coefficient of Sapphire matched reasonably well with the heterostructure which also allowed us to efficiently bond the QW heterostructure without damaging or cracking the grown epitaxial films. The resonators were then fabricated via e-beam lithography followed by inductively-coupled plasma reactive ion etching using a SiO_2 etch mask. Since the height (h) was fixed by growth, we scaled the radius ($R = 1.4 \mu m$) of the resonators to achieve the aspect ratio

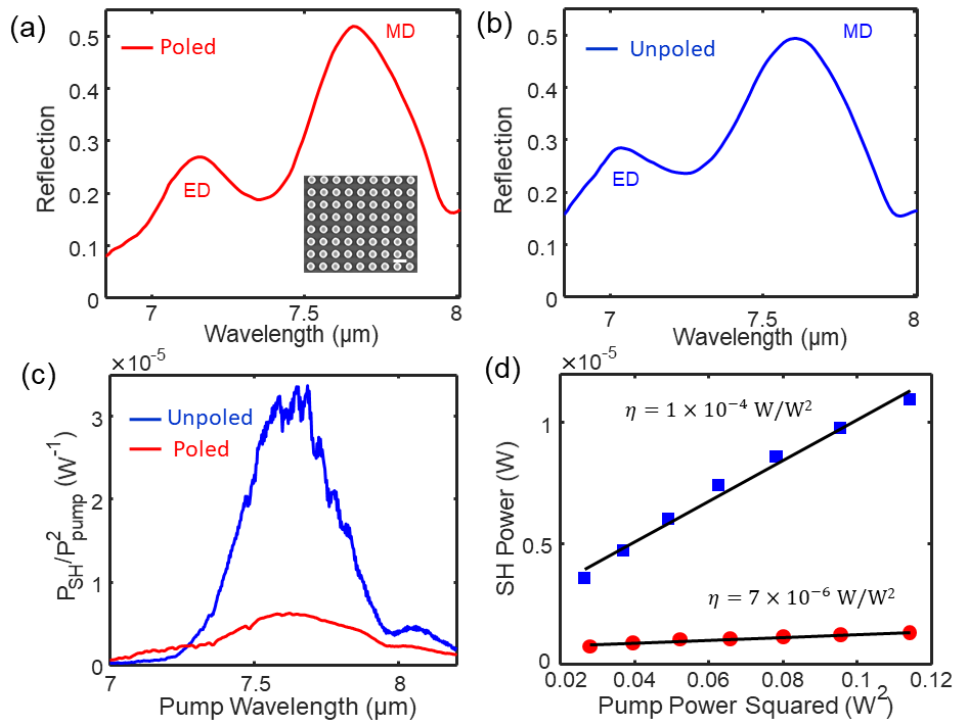


Fig. 5. Experimental linear and nonlinear measurements of SHG in reflection from fabricated metasurfaces with poled and unpoled meta-atoms. (a, b) Linear reflectance measurement of the metasurfaces with poled (a) and unpoled (b) meta-atoms with $R/h = 0.93$ and $h = 1.5 \mu\text{m}$. Both metasurfaces show similar linear reflectance spectra with the MD mode at similar wavelengths as expected and designed for. The inset shows a top view scanning electron micrograph of one of the fabricated metasurfaces. The white scale bar corresponds to 4 microns. (c) Experimentally-measured normalized SH power conversion efficiency (defined as the ratio of peak SH power to square of peak pump power) in reflection as a function of incident pump wavelength of the metasurfaces with poled (red) and unpoled (blue) meta-atoms. The metasurface with poled meta-atoms show about a factor of ~ 5 smaller SHG efficiency in reflection. The experimental results agree qualitatively well with the numerical simulations shown in Fig. 4. (d) Experimentally-measured peak SH power in reflection as function of square of incident peak pump power for the same metasurfaces as in (c) but at a fixed pump wavelength of $7.65 \mu\text{m}$. The slope of the linear fits (black solid lines) which determine the nonlinear conversion factor η is smaller for the poled case (red circles) compared to the unpoled case (blue squares).

$(R/h) = 0.93$ such that the meta-atoms support a MD mode at $\sim 7.8 \mu\text{m}$. Further details on the fabrication process can be found in Ref. 34.

Figure 5(a, b) shows the experimentally measured linear reflectance spectrum obtained using a Fourier-transform infrared spectroscopy (FTIR) microscope for both the poled and unpoled metasurfaces and the inset in Fig. 5(a) shows a top-view scanning electron micrograph of one of the fabricated metasurfaces. As expected, both metasurfaces show a similar linear response with a pronounced MD resonance near the IST wavelength of $\sim 7.8 \mu\text{m}$. Next, we experimentally measured the generated SH spectra in reflection geometry from the metasurfaces shown in Fig. 5(a, b). We chose to measure SHG in reflection geometry because, as described in Ref. 34, the transmitted SH signal gets trapped in the sapphire substrate due to total internal reflection.

For the nonlinear optical measurements, we used a tunable quantum cascade laser (QCL) as the pump. The laser was operated at 250 kHz repetition frequency with duty cycle of 10% and 1200 mA driving current. The measurements were done at normal incidence where the pump light was focused on the sample using an aspheric lens with numerical aperture of 0.85. The radius of the focused pump spot on the metasurfaces was measured by the knife-edge technique to be about 22 μm . The reflected SH light was collected using the same aspheric lens and was redirected to a calibrated InSb detector using a 2-inch focal length parabolic mirror to measure the SH power. Figure 5(c) shows the experimentally measured normalized SHG efficiency as a function of pump wavelength for both the *poled* and *unpoled* metasurfaces. As predicted by our simulations, we can clearly see that the *poled* metasurfaces have a lower SHG efficiency compared to the *unpoled* metasurfaces in reflection direction. Experimentally, we measured the difference in SHG efficiencies between the *poled* and *unpoled* metasurfaces to be about a factor of 5. This agrees qualitatively with the simulations. Small quantitative differences compared to simulations can be explained by the fact that exact geometric parameters of the fabricated meta-atoms vary slightly from numerical simulations due to fabrication imperfections. In addition, the fabricated meta-atoms have a conical shape as opposed to a cylindrical shape because of slanted sidewalls.

Finally, to confirm that the nonlinear conversion factors for both the metasurfaces are also different, we experimentally measured reflected peak SH power (P_{SH}) as function of the square of the peak pump power (P_{pump}^2). The nonlinear SH power conversion factor, $\eta = \frac{P_{SH}}{P_{pump}^2}$, is shown in Fig. 5(d). We can clearly see that the poled metasurfaces have a lower nonlinear conversion factor compared to unpoled metasurfaces in reflection.

We would like to point out while in this work, vertical poling has been found to reduce SH emission efficiency in the proposed metasurface, SH light emission can be amplified in poled meta-atoms if SH light is coupled to Mie-type modes in which the z-component of the field displays odd symmetry along the z direction. Indeed, we stress that the spatial distribution of the SH current J_z^{SH} is forced to assume odd symmetry along the z-axis in poled meta-atoms (as opposed to even symmetry for unpoled meta-atoms). This can be exploited to *enhance* the SHG efficiency by tuning the SH at the resonance wavelength of any Mie-type mode with odd symmetry. In fact, this behavior can be observed in the proposed metasurface with $R/h = 0.87$

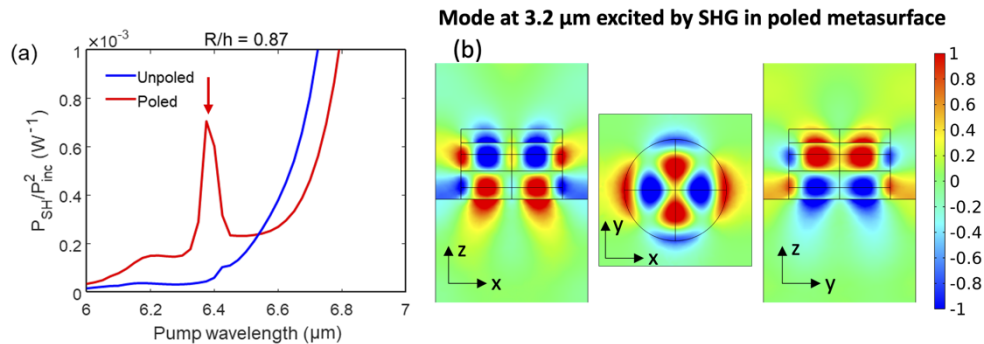


Fig. 6. Nonlinear numerical simulations of the metasurface with $R/h=0.87$ comprised of the poled and unpoled meta-atoms (a) Comparison of numerically calculated reflected normalized SH power conversion efficiency (defined as the ratio of the SH power emitted to square of the pump power) from metasurfaces with poled and unpoled meta-atoms with $R/h=0.87$. In this case, metasurfaces with unpoled meta-atoms in general have lower SHG efficiency compared to poled meta-atoms for pump wavelength $\sim 6.4 \mu\text{m}$. (b) Spatial distribution of the SH z-component of the electric field (E_z) when the pump is tuned at $\sim 6.4 \mu\text{m}$ for the poled metasurface (peak of the red curve in (a) and shown by the red arrow).

when the pump is at $\sim 6.4 \mu\text{m}$. Figure 6(a) shows that for pump wavelengths $\sim 6.4 \mu\text{m}$, albeit with a magnitude smaller than the peak at $\sim 7.5 \mu\text{m}$ (reported in Fig. 4 and 5), we do see a significant enhancement of SHG efficiency for poled metasurfaces compared to unpoled structures. This enhancement provided by vertical poling originates from the fact that the meta-atom supports a Mie-type mode at $\sim 3.2 \mu\text{m}$ with odd symmetry for the z -component of the electric field (Fig. 6(b)). When the structure is pumped at $\sim 6.4 \mu\text{m}$, SH light couples to this odd-symmetry mode only if the meta-atom is poled, while the mode remains dark in the SH spectrum if the meta-atom is unpoled. The excitation of this odd-symmetry mode at $\sim 3.2 \mu\text{m}$ via SHG in the poled structure is illustrated in Fig. 6(b), in which the spatial distribution of the SH E_z field near and within the meta-atom is reported. The excitation is forbidden in the unpoled metasurface. These results show that poling can be regarded as a tool to improve spatial overlap and mode matching for frequency mixing in photonic nanostructures, and that the presented technique adds an additional degree of freedom in optimizing SHG from nonlinear all-dielectric metasurfaces.

4. Conclusion

To conclude, we have demonstrated that the polarity of $\chi^{(2)}$ can be utilized as a new degree of freedom to control and enhance SHG from all-dielectric metasurfaces. This degree of freedom can be exploited in all-dielectric intersubband metasurfaces that constitute Mie-type resonators with multi-QW heterostructures embedded within it that support quantum engineered intersubband transitions. As a proof-of-concept, we designed and fabricated two types of metasurfaces, where in the first case, the meta-atoms are made out of nonlinear material with a single polarity of $\chi^{(2)}$ and in the second case the meta-atoms are made out of nonlinear material with opposite polarities of $\chi^{(2)}$. Because of different spatial distribution of the nonlinear polarization within the meta-atoms, for both cases, different modes or superposition of modes at the second-harmonic wavelength are excited which leads to different emission patterns of second-harmonic signal leading to overall different second-harmonic generation efficiencies.

While we demonstrated difference in SHG efficiency for these two simple geometries, we envision that this approach can be extended to more complex geometries and photonic modes as well as for operation in transmission direction. In particular, this approach can be useful in optimizing the nonlinear overlap integrals [20], for controlling the Mie mode that is excited at the SH wavelength and, also control the SHG radiation pattern. Our approach can therefore offer exciting new opportunities for studying nonlinear wave mixing using all-dielectric metasurfaces and for developing ultrathin and efficient classical or quantum light sources [4,5] for various applications ranging from sensing [3], spectroscopy [1], to hyperspectral infrared imaging [2].

Funding. Basic Energy Sciences; Defense Advanced Research Projects Agency; Ministero dell'Istruzione, dell'Università e della Ricerca.

Acknowledgments. This work was supported by the U.S. Department of Energy, Office of Basic Energy Sciences, Division of Materials Sciences and Engineering and performed, in part, at the Center for Integrated Nanotechnologies, an Office of Science User Facility operated for the U.S. Department of Energy (DOE) Office of Science. Sandia National Laboratories is a multi-mission laboratory managed and operated by National Technology and Engineering Solutions of Sandia, LLC, a wholly owned subsidiary of Honeywell International, Inc., for the U.S. Department of Energy's National Nuclear Security Administration under contract DE-NA0003525. The University of Texas and the Technical University of Munich members of the team acknowledges financial support from the DARPA NASCENT program. This paper describes objective technical results and analysis. Any subjective views or opinions that might be expressed in the paper do not necessarily represent the views of the U.S. Department of Energy or the United States Government. The University of Brescia team members were partly supported by MIUR (Italian Minister for Education) under the initiative "Departments of Excellence" (Law 232/2016).

Disclosures. The authors declare no conflicts of interest.

Data availability. The data that support the findings of this study are available from the corresponding authors upon reasonable request

References

1. J. Haas and B. Mizaikoff, "Advances in Mid-Infrared Spectroscopy for Chemical Analysis," *Annu. Rev. Anal. Chem.* **9**(1), 45–68 (2016).
2. M. Hermes, R. B. Morrish, L. Huot, L. Meng, S. Junaid, J. Tomko, G. R. Lloyd, W. T. Masselink, P. Tidemand-Lichtenberg, and C. Pedersen, "Mid-IR Hyperspectral Imaging for Label-Free Histopathology and Cytology," *J. Opt.* **20**(2), 023002 (2018).
3. D. Jung, S. Bank, M. L. Lee, and D. Wasserman, "Next-Generation Mid-Infrared Sources," *J. Opt.* **19**(12), 123001 (2017).
4. T. Santiago-Cruz, A. Fedotova, V. Sultanov, M. A. Weissflog, D. Arslan, M. Younesi, T. Pertsch, I. Staude, F. Setzpfandt, and M. Chekhova, "Photon Pairs from Resonant Metasurfaces," *Nano Lett.* **21**(10), 4423–4429 (2021).
5. T. Santiago-Cruz, S. D. Gennaro, O. Mitrofanov, S. Addamane, J. Reno, I. Brener, and M. Chekhova, "Resonant Semiconductor Metasurfaces for Generating Complex Quantum States," Arxiv. 2204.10371 (2022).
6. D. Sun, Y. Zhang, D. Wang, W. Song, X. Liu, J. Pang, D. Geng, Y. Sang, and H. Liu, "Microstructure and Domain Engineering of Lithium Niobate Crystal Films for Integrated Photonic Applications," *Light: Sci. Appl.* **9**(1), 197 (2020).
7. M. M. Fejer, G. A. Magel, D. H. Jundt, and R. L. Byer, "Quasi-Phase-Matched Second Harmonic Generation: tuning and tolerances," *IEEE J. Quantum Electron.* **28**(11), 2631–2654 (1992).
8. M. H. Chou, I. Brener, M. M. Fejer, E. E. Chaban, and S. B. Christman, "1.5- μm -band Wavelength Conversion based on Cascaded Second-Order Nonlinearity in LiNbO₃ Waveguides," *IEEE Photonics Technol. Lett.* **11**(6), 653–655 (1999).
9. A. S. Helmy, "Recent Advances in Phase Matching of Second-Order Nonlinearities in Monolithic Semiconductor Waveguides," *Laser Photonics Rev.* **5**(2), 272–286 (2011).
10. I. Brener, S. Liu, I. Staude, J. Valentine, and C. Holloway, *Dielectric Metamaterials: Fundamentals, Designs and Applications*, Woodhead Publishing, (2019).
11. Y. Kivshar, "All-Dielectric Meta-Optics and Non-Linear Nanophotonics," *National Science Rev.* **5**(2), 144–158 (2018).
12. S. Liu, M. B. Sinclair, S. Saravi, G. A. Keeler, Y. Yang, J. Reno, G. M. Peake, F. Setzpfandt, I. Staude, T. Pertsch, and I. Brener, "Resonantly Enhanced Second-Harmonic Generation Using III-V Semiconductor All-Dielectric Metasurfaces," *Nano Lett.* **16**(9), 5426–5432 (2016).
13. S. Liu, P. P. Vabishchevich, A. Vaskin, J. L. Reno, G. A. Keeler, M. B. Sinclair, I. Staude, and I. Brener, "An All-Dielectric Metasurface as a Broadband Optical Frequency Mixer," *Nat. Commun.* **9**(1), 2507 (2018).
14. R. Camacho-Morales, M. Rahmani, S. Kruk, L. Wang, L. Xu, D. A. Smirnova, A. S. Solntsev, A. Miroshnichenko, H. H. Tan, F. Karouta, S. Naureen, K. Vora, L. Carletti, C. D. Angelis, C. Jagadish, Y. S. Kivshar, and D. N. Neshev, "Nonlinear Generation of Vector Beams from AlGaAs Nanoantennas," *Nano Lett.* **16**(11), 7191–7197 (2016).
15. E. V. Melik-Gaykazyan, K. L. Koshelev, J. H. Choi, S. S. Kruk, H. G. Park, A. A. Fedyanin, and Y. S. Kivshar, "Enhanced Second-Harmonic Generation with Structured Light in AlGaAs Nanoparticles Governed by Magnetic Response," *JETP Lett.* **109**(2), 131–135 (2019).
16. P. P. Vabishchevich, S. Liu, M. B. Sinclair, G. A. Keeler, G. M. Peake, and I. Brener, "Enhanced Second-Harmonic Generation Using Broken Symmetry III-V Semiconductor Fano Metasurfaces," *ACS Photonics* **5**(5), 1685–1690 (2018).
17. Z. Liu, Y. Xu, Y. Lin, J. Xiang, T. Feng, Q. Cao, J. Li, S. Lan, and J. Liu, "High-Q Quasibound States in the Continuum for Nonlinear Metasurfaces," *Phys. Rev. Lett.* **123**(25), 253901 (2019).
18. K. Koshelev, S. Kruk, E. M. Gaykazyan, J. H. Choi, A. Bogdanov, H. G. Park, and Y. Kivshar, "Subwavelength Dielectric Resonators for Nonlinear Nanophotonics," *Science* **367**(6475), 288–292 (2020).
19. A. P. Anthur, H. Zhang, R. P. Dominguez, D. A. Kalashnikov, S. T. Ha, T. W. W. MaB, A. I. Kuznetsov, and L. Krivitsky, "Continuous Wave Second Harmonic Generation Enabled by Quasi-Bound-States in the Continuum on Gallium Phosphide Metasurfaces," *Nano Lett.* **20**(12), 8745–8751 (2020).
20. L. Carletti, A. Locatelli, O. Stepanenko, G. Leo, and C. D. Angelis, "Enhanced Second-Harmonic Generation from Magnetic Resonance in AlGaAs Nanoantennas," *Opt. Express* **23**(20), 26544–26550 (2015).
21. F. J. F. Lochner, A. N. Fedotova, S. Liu, G. A. Keeler, G. M. Peake, S. Saravi, M. R. Shcherbakov, S. Burger, A. A. Fedyanin, I. Brener, T. Pertsch, F. Setzpfandt, and I. Staude, "Polarization-Dependent Second Harmonic Diffraction from Resonant GaAs Metasurfaces," *ACS Photonics* **5**(5), 1786–1793 (2018).
22. J. D. Sautter, L. Xu, A. E. Miroshnichenko, M. Lysevych, I. Volkovskaya, D. A. Smirnova, R. Camacho-Morales, K. Z. Kamali, F. Karouta, K. Vora, H. H. Tan, M. Kauranen, I. Staude, C. Jagadish, D. N. Neshev, and M. Rahmani, "Tailoring Second-Harmonic Emission from (111)-GaAs Nanoantennas," *Nano Lett.* **19**(6), 3905–3911 (2019).
23. L. Xu, G. Saerens, M. Timofeeva, D. A. Smirnova, I. Volkovskaya, M. Lysevych, R. Camacho-Morales, M. Cai, K. Z. Kamali, L. Huang, F. Karouta, H. H. Tan, C. Jagadish, A. E. Miroshnichenko, R. Grange, D. N. Neshev, and M. Rahmani, "Forward and Backward Switching of Nonlinear Unidirectional Emission from GaAs Nanoantennas," *ACS Nano* **14**(2), 1379–1389 (2020).
24. G. Marino, D. Rocco, C. Gigli, G. Beaudoin, K. Pantzas, S. Suffit, P. Filloux, I. Sagnes, G. Leo, and C. D. Angelis, "Harmonic Generation with Multi-Layer Dielectric Metasurfaces," *Nanophotonics* **10**(7), 1837–1843 (2021).
25. L. Carletti, A. Locatelli, D. Neshev, and C. D. Angelis, "Shaping the Radiation Pattern of Second-Harmonic Generation from AlGaAs Dielectric Nanoantennas," *ACS Photonics* **3**(8), 1500–1507 (2016).

26. K. Frizyuk, "Second-harmonic generation in dielectric nanoparticles with different symmetries," *J. Opt. Soc. Am. B* **36**(8), F32–F37 (2019).
27. D. Rocco, C. Gigli, L. Carletti, G. Marino, M. A. Vincenti, G. Leo, and C. D. Angelis, "Vertical Second Harmonic Generation in Asymmetric Dielectric Nanoantennas," *IEEE Photonics J.* **12**(3), 1–7 (2020).
28. L. Xu, M. Rahmani, D. Smirnova, K. Z. Kamali, G. Zhang, D. Neshev, and A. E. Miroshnichenko, "Highly-Efficient Longitudinal Second-Harmonic Generation from Doubly-Resonant AlGaAs Nanoantennas," *Photonics* **5**(3), 29 (2018).
29. J. Lee, M. Tymchenko, C. Argyropoulos, P. Chen, F. Lu, F. Demmerle, G. Boehm, M. C. Amann, A. Alu, and M. A. Belkin, "Giant Nonlinear Response from Plasmonic Metasurfaces Coupled to Intersubband Transitions," *Nature* **511**(7507), 65–69 (2014).
30. J. Lee, N. Nookala, J. S. Gomez-Diaz, M. Tymchenko, F. Demmerle, G. Boehm, M. C. Amann, A. Alu, and M. A. Belkin, "Ultrathin Second-Harmonic Metasurfaces with Record-High Nonlinear Optical Response," *Adv. Opt. Mater.* **4**(5), 664–670 (2016).
31. O. Wolf, S. Campione, A. Benz, A. P. Ravikumar, S. Liu, T. S. Luk, E. A. Kadlec, E. A. Shaner, J. F. Klem, M. B. Sinclair, and I. Brener, "Phased-Array Sources Based on Nonlinear Metamaterial Nanocavities," *Nat. Commun.* **6**(1), 7667 (2015).
32. R. Sarma, D. de Ceglia, N. Nookala, M. A. Vincenti, S. Campione, O. Wolf, M. Scalora, M. B. Sinclair, M. A. Belkin, and I. Brener, "Broadband and Efficient Second-Harmonic Generation from a Hybrid Dielectric Metasurface/Semiconductor Quantum-Well Structure," *ACS Photonics* **6**(6), 1458–1465 (2019).
33. R. Sarma, J. Xu, D. de Ceglia, L. Carletti, S. Campione, J. Klem, M. B. Sinclair, M. A. Belkin, and I. Brener, "An All-Dielectric Polaritonic Metasurfaces with a Giant Nonlinear Optical Response," *Nano Lett.* **22**(3), 896–903 (2022).
34. N. Nookala, J. Xu, O. Wolf, S. March, R. Sarma, S. Bank, J. Klem, I. Brener, and M. Belkin, "Mid-Infrared Second-Harmonic Generation in Ultra-Thin Plasmonic Metasurfaces without a Full-Metal Backplane," *Appl. Phys. B* **124**(7), 132 (2018).
35. S. Liu, G. A. Keeler, J. L. Reno, M. B. Sinclair, and I. Brener, "III-V Semiconductor Nanoresonators – A New Strategy for Passive, Active, and Nonlinear All-Dielectric Metamaterials," *Adv. Opt. Mater.* **4**(10), 1457–1462 (2016).
36. E. Rosencher, A. Fiore, B. Vinter, V. Berger, P. H. Bois, and J. Nagle, "Quantum Engineering of Optical Nonlinearities," *Science* **271**(5246), 168–173 (1996).
37. F. Capasso, C. Sirtori, and A. Cho, "Coupled Quantum Well Semiconductors with Giant Electric Field Tunable Nonlinear Optical Properties in the Infrared," *IEEE J. Quantum Electron.* **30**(5), 1313–1326 (1994).
38. R. Sarma, N. Nookala, K. J. Reilly, S. Liu, D. de Ceglia, L. Carletti, M. D. Goldflam, S. Campione, K. Sapkota, H. Green, G. T. Wang, J. Klem, M. B. Sinclair, M. A. Belkin, and I. Brener, "Strong Coupling in All-Dielectric intersubband Polaritonic Metasurfaces," *Nano Lett.* **21**(1), 367–374 (2021).